Topology optimization of supports with imperfect bonding in additive manufacturing

Grégoire Allaire, Beniamin Bogosel, Matías Godoy

Topology optimization of supports with imperfect bonding in additive manufacturing

Grégoire Allaire, Beniamin Bogosel, Matías Godoy[1]

[1]CMAP, Ecole Polytechnique, CNRS, Institut Polytechnique de Paris, 91128 Palaiseau, France. gregoire.allaire@polytechnique.fr

Abstract

Supports are an important ingredient of the building process of structures by additive manufacturing technologies. They are used to reinforce overhanging regions of the desired structure and/or to facilitate the mitigation of residual thermal stresses due to the extreme heat flux produced by the source term (laser beam). Very often, supports are, on purpose, weakly connected to the built structure for easing their removal. In this work we consider an imperfect interface model for which the interaction between supports and the built structure is not ideal, meaning that the displacement is discontinuous at the interface while the normal stress is continuous and proportional to the jump of the displacement. The optimization process is based on the level set method, body fitted meshes and the notion of shape derivative using the adjoint method. We provide 2-d and 3-d numerical examples, as well as a comparison with the usual perfect interface model. Completely different designs of supports are obtained with perfect or imperfect interfaces.

Keywords: Imperfect interface, interfacial rigidity, support optimization, topology optimization, level set method

1 Introduction

Additive manufacturing (AM) is the set of processes for building objects using a layer by layer deposition system. This is an active field due mainly to the provided advantages: the complexity of the structures is almost unlimited from a geometrical point of view (given mostly by the width of layers) in comparison with classical methods such as moulding or casting [12, 28], in particular referring to the possible shapes and topologies involved. Applications of AM can be seen in diverse industries such as aeronautics, automotive or biomedical, among others.

Despite these advantages, AM has certain issues that should be addressed in order to ensure the conformity of the printed structures. As pointed out in many works (see [4, 15, 23, 26, 33, 34, 38, 47] and references therein) there are two main issues. The first one is concerned with so-called *overhangs*, which are defined as parts of the structure to be fabricated with large near-horizontal surfaces (with respect to the build direction, assumed vertical in this article). The presence of overhangs may lead to undesired distortions related to the lack of support for the melted powder. The second issue is related to an uneven temperature distribution in the built part during the fabrication process. Since the melting is performed by a laser (or electron) beam, a high temperature gradient is observed in the structure, which induces thermal residual stresses and therefore unexpected distortion of

the desired design. In order to deal with these issues, a common practice is to introduce *supports*, namely sacrificial material which is added to the built part to improve its behavior during the building process but which is removed after completion.

Supports can ensure that overhanging regions are built correctly and they can act as a thermal sink to ease the evacuation of heat. Since support structures are removed after the fabrication process is finished, they should be designed such that their removal is facilitated and does not alter contact regions with the fabricated part [12, 26, 28]. Quite often in practice, supports feature a contact zone with the built part which is jagged, with many small indentations or holes, or has a tree-like structure. It has the effect that the supports are weakly connected to the built part and therefore are easier to remove in the end.

In order to minimize production costs given by the duration of the fabrication process and the metallic powder consumption, it is meaningful to optimize support structures in order to minimize their volume while not degrading their mechanical performance. Several previous works used shape and topology optimization techniques in order to optimize supports (see [3, 4, 13, 27, 38, 37, 43, 44] among others). Other works focus on particular types of supports, like sloping wall structures [33], tree-like structures [26, 48], scaffolds [24] and others [34, 47]. Of course, it is possible to optimize simultaneously the built part and its supports, eventually up to the point that the part becomes self-supported. We shall not discuss this alternative approach here and refer to previous works [7, 9] and references therein. A common characteristic of all these works is the assumption that the interface between supports and the built part is perfect, i.e. the bonding between them has no defects or gaps, which means that classical transmission conditions (continuity of displacement and normal stress) can used at the interface separating the part and its supports.

Our first main contribution in the present work, motivated by examples observed in practice, is to consider a model where the part-support interface is imperfect. This is modeled by considering a spring-type interfacial condition as already used in many previous works [1, 35, 40, 41, 42, 50]. The interface condition relates the jump of the discontinuous displacement across the interface to the normal stress which remains continuous (see (2.8) for details). This linear dependence involves two constitutive parameters representing the degree of adhesion between the part and the support, or equivalently the stiffness of the interface. These two parameters are related to interfacial rigidity in the normal and tangential directions. In [1] this type of condition is used in order to model several possible imperfections in the bonding for reinforced composite structures (such as a lubricated bonding or a total debonding). In the same vein, optimal properties of composite materials, with such imperfect bonding interfacial condition, were obtained in [40, 41, 42].

Our second main contribution is to optimize the geometry and topology of these imperfectly bonded supports. Because of our motivation in AM, we do not consider a general two-phase optimal design, as in our previous work in the conductivity setting [5] (with an imperfect interface). Rather, the built part is kept fixed while only the support is optimized. In particular, the interface between them does not change in its normal direction (it can only extend or retract in a tangential direction): this makes the differentiation process simpler. The goal of our support optimization is to improve the mechanical performance during the AM process, linked to the occurence of overhanging surfaces and thermal deformations, in order to ensure the quality of the built part as an ultimate purpose. Our main theoretical ingredient is the notion of shape derivative, in the sense of Hadamard [2, 19, 32]. Our main numerical ingredient is the level set method [46]. This is, by now, a classical setting for shape and topology optimization [10, 8].

The paper is organized as follows. In Section 2, the mechanical model, the optimization problem and two loading cases (for our numerical examples) are discussed. The two loads are either pseudo-gravity forces or equivalent thermal forces. In both cases, the objective function is the compliance. In Section 3 the shape derivatives of the objective functions are established, which is not standard because of the imperfect interface condition. In Section 4 we present the numerical framework used in the simulations. In particular, since the part is fixed during the optimization process, its boundary, containing the interface with the support, is meshed exactly. Since the displacements are discontinuous through this interface, the finite element discretization requires some special care. We propose a simple penalization/extension approach which is an alternative to other well-known approaches such as Discontinuous Galerkin methods or extended finite element methods, not always implemented in typical finite element softwares. Section 5 is devoted to 2-d and 3-d numerical experiments that asses the relevance of our approach for support optimization. In particular, our optimized supports are systematically compared to their counterparts for a perfect interface. Very often, completely different designs of supports are obtained with perfect or imperfect interfaces. The role of the anisotropy of the interface (tangential versus normal rigidity) is also clearly demonstrated. Finally Section 6 draws some conclusions and perspectives. In particular, our work is a first step in the design of optimized imperfectly bonded supports and some of our results may be difficult to achieve in practice. It requires some further work which is briefly discussed.

2 Problem Setting

2.1 Mechanical model

Consider a shape ω and a support S (which may have several connected components), both being disjoint piecewise smooth bounded open sets of $\mathbb{R}^d$ ($d = 2$ or $d = 3$). The domains ω and S are made of isotropic materials (without necessarily the same mechanical properties). In this work the shape ω is fixed and only the supports S are subject to optimization. The total structure is denoted $\Omega = S \cup \omega$ and is assumed to be contained in a rectangular or computational domain D, which models the *build chamber* (see Figure 1). The baseplate is the bottom boundary of D and is denoted $\Gamma_D := \{x \in D : x_d = 0\}$, where the build direction is vertical along x_d. Except otherwise mentioned, the supports are clamped to the baseplate Γ_D. The other regions of the boundary of the supported structure Ω are traction free, denoted by Γ_N.

In the following some specific functional spaces are required in order to define a proper mathematical formulation. For a boundary $\gamma \subset \partial\Omega$, we define the Broken Sobolev spaces of displacements, which are *discontinuous* through the interface $\Gamma := \partial S \cap \partial\omega$ between ω and S, by

$$H^1_b(\Omega;\omega,S)^d := \left\{ u \in L^2(\Omega)^d : \ u_S = u|_S \in H^1(S)^d, \ u_\omega = u|_\omega \in H^1(\omega)^d \right\}, \tag{2.1}$$

$$H^1_{b,\gamma}(\Omega;\omega,S)^d := \left\{ u \in H^1_b(\Omega;\omega,S)^d : \ u = 0 \text{ on } \gamma \right\}. \tag{2.2}$$

In order to simplify the notation, for the boundary Γ_D (the baseplate) the broken spaces are denoted by

$$\mathbf{X} := H^1_b(\Omega;\omega,S)^d \ \text{ and } \ \mathbf{X}_0 := H^1_{b,\Gamma_D}(\Omega;\omega,S)^d. \tag{2.3}$$

Under this notation, a displacement $u \in \mathbf{X}$ can be written

$$u = u_\omega \chi_\omega + u_S \chi_S,$$

where $\chi_{\mathcal{O}}$ is the characteristic function of the set $\mathcal{O}$, and $u_\omega \neq u_S$ on the interface Γ in full generality. These spaces are endowed with the so-called *broken norm*:

$$\|v\|_{\mathbf{X}} := \left(\|v_\omega\|^2_{H^1(\omega)} + \|v_S\|^2_{H^1(S)}\right)^{1/2}, \tag{2.4}$$

which make them Hilbert spaces (see [20, 22] for further details).

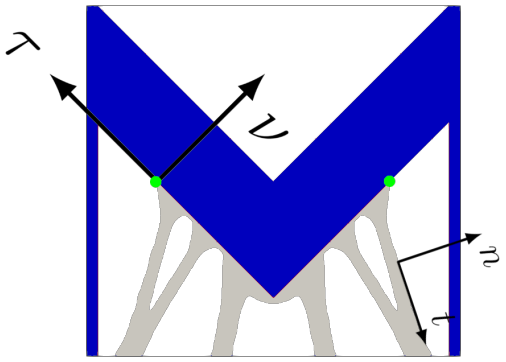

Figure 1: An M-part ω (in blue) with its supports S (in grey) inside a squared build chamber D. On the interface $\Gamma = \partial S \cap \partial\omega$ the unit normal vector is ν and the tangential one is τ. The two green points are the boundary $\partial(\partial S \cap \partial\omega)$ of the interface. On the support free boundary $\partial S \setminus \partial\omega$ the unit normal vector is n and the tangential one is t.

We choose an orientation on the interface $\Gamma = \partial S \cap \partial\omega$ such that the normal vector $\nu = n_S$ points outwards S (see Figure 1) and we define the jump $[\cdot]$ across the interface Γ for a function f by

$$[f] = f_S - f_\omega. \tag{2.5}$$

The *strain tensor* e is $e(u) = \dfrac{1}{2}\left(\nabla u + \nabla u^T\right)$ and the *stress tensor* σ is defined via Hooke's law by

$$\sigma(u) = Ae(u) = 2\mu e(u) + \lambda \operatorname{tr}\left(e(u)\right) \mathrm{Id} \; = 2\mu e(u) + \lambda \operatorname{div} u \, \mathrm{Id}\,, \tag{2.6}$$

where μ and λ are the Lamé coefficients. In order to take into account the possibility that the part and support may have different material properties we consider

$$A = A_\omega \chi_\omega + A_S \chi_S \quad \text{or} \quad \mu = \mu_\omega \chi_\omega + \mu_S \chi_S, \;\; \lambda = \lambda_\omega \chi_\omega + \lambda_S \chi_S,$$

with constant properties in ω and in S. The elastic displacement u of the supported structure $\Omega = \omega \cup S$ is the unique solution in the space $\mathbf{X}_0$ to the following variational problem (see [35]):

$$\begin{cases} \text{Find } u \in \mathbf{X}_0, \text{ such that, for all } v \in \mathbf{X}_0, \\ \displaystyle\int_\omega \sigma(u_\omega) : e(v_\omega)\, dx + \int_S \sigma(u_S) : e(v_S)\, dx + \int_\Gamma R^{-1}[u] \cdot [v]\, ds = L(v), \end{cases} \tag{2.7}$$

where L is a linear functional on $\mathbf{X}$ representing the action of forces on the structure and to be specified for each case of interest.

In (2.7) R denotes a second order tensor representing the compliance (or inverse of the rigidity) of the interface $\Gamma = \partial S \cap \partial\omega$ between the part and the supports. The interface

can have different rigidities in the normal and tangential directions, so R has the following form:

$$R = \alpha(I - \nu \otimes \nu) + \beta \nu \otimes \nu, \text{ or } R_{ij} = \alpha(\delta_{ij} - \nu_i \nu_j) + \beta \nu_i \nu_j,$$

with the inverse given by

$$R^{-1} = \frac{1}{\alpha}(I - \nu \otimes \nu) + \frac{1}{\beta} \nu \otimes \nu, \text{ or } R^{-1}_{ij} = \frac{1}{\alpha}(\delta_{ij} - \nu_i \nu_j) + \frac{1}{\beta} \nu_i \nu_j,$$

where $\alpha \geq 0, \beta \geq 0$ are parameters denoting the compliance in the tangential and normal directions of the interface respectively. The boundary integral term in (2.7) corresponds to the following transmission condition on the interface

$$[u] = -R\sigma(u) \cdot \nu \quad \text{on} \quad \Gamma. \tag{2.8}$$

This interface condition models the imperfection on the interface or, alternatively, the degree of adhesion between ω and S. As already said, it is a classical spring-like condition [1, 35, 40, 41, 42, 50].

For $\alpha > 0, \beta > 0$ (i.e. for R non-singular), it has been proved (see [39, 30]) that, for any $L \in \mathbf{X}'$, the variational problem (2.7) has a unique solution $u \in \mathbf{X}_0$.

Assumption 2.1. *In the following, we assume that the solution u of system (2.7) is smooth in each sub-domain, namely $u_S = u|_S \in H^2(S)^d, u_\omega = u|_\omega \in H^2(\omega)^d$. This assumption can be justified if the forces and the interface Γ are smooth. The only difficulty comes from the possible junction between Γ_D and Γ_N. Indeed, it is well known that at points in $\overline{\Gamma}_D \cap \overline{\Gamma}_N$ the solution u may feature a singularity such that it does not belong to H^2 on each subdomain. We exclude this possibility that creates technical difficulties which are not at the core of our study. Assuming, for example, that Γ_D and Γ_N are two different connected components of ∂D no such singular behavior can occur.*

Remark 2.2. *(i) If $\alpha = \beta$ then $R^{-1} = \frac{1}{\alpha} I$, which can be interpreted as a penalization for the jump $[u]$ in the variational formulation. Letting $\alpha \to 0^+$, it is expected that $[u]$ goes to zero and, in the limit, a perfect transmission condition at the interface Γ is obtained. A proof for scalar case can be found in [5]. In this limit case, the variational formulation becomes*

$$\begin{cases} \text{Find } u \in \left(H^1_{\Gamma_D}\right)^d, \text{ such that, for all } v \in \left(H^1_{\Gamma_D}\right)^d, \\ \displaystyle\int_\omega \sigma(u_\omega) : e(v_\omega)\, dx + \int_S \sigma(u_S) : e(v_S)\, dx = L(v), \end{cases} \tag{2.9}$$

where $H^1_{\Gamma_D} := \left\{u \in H^1(\Omega) : \ u = 0 \text{ on } \Gamma_D\right\}$ is the classical Sobolev space (in particular $[u] = 0$ across Γ).

(ii) We can extend the variational formulation for the case where R is singular by defining

$$M = \begin{cases} R^{-1} & \text{if } \alpha > 0, \ \beta > 0, \\ \alpha^{-1}(I - \nu \otimes \nu) & \text{if } \alpha > 0, \ \beta = 0, \\ \beta^{-1} \nu \otimes \nu & \text{if } \alpha = 0, \ \beta > 0, \\ 0 & \text{if } \alpha = 0, \ \beta = 0. \end{cases}$$

As stated in [29], the space of definition for (2.7) is

$$\mathbf{Y} := \{v \in \mathbf{X} : \ [v] = MR[v] \text{ on } \Gamma\}.$$

For example, if $\alpha = 0, \beta = 0$ we obtain $\mathbf{Y} = H^1(\Omega)^d$ (as $[u] = 0$ in Γ), if $\alpha > 0, \beta > 0$ we have $\mathbf{Y} = \mathbf{X}$ and for $\alpha = 0$ or $\beta = 0$, $\mathbf{Y}$ is strictly contained in $\mathbf{X}$ with a constraint given by $[v] = MR[v]$. In the rest of the paper we only consider the non-singular case.

We consider an optimization problem where the optimization variable is the support S, while the shape ω is fixed. It reads

$$\min_{S\in\mathcal{U}_{ad},\,|S|=V_{sup}} J(S),$$

where V_{sup} is a target volume for the supports and $\mathcal{U}_{ad}$ is the set of admissible supports

$$\mathcal{U}_{ad} := \{S \subset (D \setminus \omega) \text{ such that, } \Gamma_D \cap \partial(S \cup \omega) \neq \emptyset,\ \partial\omega \cap \partial S \neq \emptyset\}.$$

The objective function is the compliance, or work done by the load, given by

$$J(S) = L(u(S), S), \tag{2.10}$$

where L is the linear form which is the right hand side of (2.7) and $u(S)$ denotes the solution of (2.7) which obviously depends on S. Note that L may also depend on S, on top of $u(S)$ (for example, if it is an integral on S).

Remark 2.3. *The simultaneous optimization of the part ω and the supports S can also be considered. It yields some additional difficulties since the interface, where the imperfect transmission condition applies, would be variable during optimization. We refer to [4] for such a study in the context of a scalar diffusion model.*

We now present the two different cases of forces or linear forms L studied in this work.

2.2 Load 1: structure under its own weight

We consider gravity-like forces for the structure ω, neglecting the weight of the supports, as is done in [4]. More precisely, the right hand side of (2.7) is

$$L(v) = \int_\omega \rho g \cdot v_\omega \, dx,$$

where ρ is the constant density of the material in ω and $g = (0, ..., 0, -1)^T$. The strong form of (2.7) is then:

$$\left\{\begin{array}{rcll} -\mathrm{div}\,(\sigma(u_\omega)) &=& \rho g & \text{in } \omega \\ u_\omega &=& 0 & \text{on } \Gamma_D \cap \partial\omega \\ \sigma(u_\omega)n &=& 0 & \text{on } \Gamma_N \cap \partial\omega \\ [\sigma(u)n] &=& 0 & \text{on } \Gamma \\ [u] &=& -R\sigma(u)\cdot\nu & \text{on } \Gamma \end{array}\right.,$$

and

$$\left\{\begin{array}{rcll} -\mathrm{div}\,(\sigma(u_S)) &=& 0 & \text{in } S \\ u_S &=& 0 & \text{on } \Gamma_D \cap \partial S \\ \sigma(u_S)n &=& 0 & \text{on } \Gamma_N \cap \partial S \\ [\sigma(u)n] &=& 0 & \text{on } \Gamma \\ [u] &=& -R\sigma(u)\cdot\nu & \text{on } \Gamma \end{array}\right.,$$

where $\sigma(u)$ is defined by (2.6).

2.3 Load 2: thermoelastic equivalent force

Because of the fabrication process, the shape ω may feature residual thermal stresses. A complete thermo-mechanical simulation of ω is performed and the deformation of the built part is computed. Based on this deformation, an equivalent thermoelastic force f_{th} supported on the interface is computed like in [3] and is used to define the linear form L in the right hand side of (2.7). Actually, at least two different L can be defined.

First, the equivalent thermoelastic force f_{th} can act only on one side of the interface, and more precisely on the side of the part ω:

$$L(v) := \int_{\partial\omega} f_{th} \cdot v_\omega \, ds, \tag{2.11}$$

which amounts to claim that the residual thermal stress affects only the built part. Replacing this formula in (2.7), by integration by parts, the following transmission conditions on the interface are obtained:

$$\begin{cases} [\sigma(u)\nu] = f_{th} & \text{on } \Gamma, \\ \sigma(u_\omega)\nu = -R^{-1}[u] - f_{th} & \text{on } \Gamma. \end{cases}$$

Secondly, the equivalent thermoelastic force f_{th} can be equally distributed to S and ω at their interface, meaning that the residual thermal stress affects both sides of the interface. It implies

$$L(v, S) := \int_{\partial\omega\setminus\partial S} f_{th} \cdot v_\omega \, ds + \int_{\partial S\cap\partial\omega} f_{th} \cdot \left(\frac{v_S + v_\omega}{2}\right) ds, \tag{2.12}$$

where one can notice that f_{th} is restricted to the ω-side of the interface if there is no support on the other side. By integration by parts in (2.7), this choice of L corresponds to the following transmission conditions on the interface

$$\begin{cases} [\sigma(u)\nu] = f_{th} & \text{on } \Gamma, \\ \sigma(u_\omega)\nu = -R^{-1}[u] - \frac{1}{2} f_{th} & \text{on } \Gamma. \end{cases}$$

3 Shape-sensitivity analysis

3.1 Preliminaries

To minimize the objective function $J(S)$, defined by (2.10), its gradient, called shape derivative, is required for implementing gradient-descent algorithms [10]. It is computed by means of the Hadamard boundary variation method [32]. Recall that the support S is included in the fixed domain D, which also contains the part ω, and that the support S does not intersect ω. Therefore, to comply with these constraints, we introduce the following set of admissible deformations

$$\Theta_{ad} := \left\{\theta \in W^{1,\infty}(D, \mathbb{R}^d) : \ \|\theta\|_{W^{1,\infty}} < 1, \ \theta \cdot n_\omega = 0 \text{ on } \partial\omega, \ \theta \cdot n_D = 0 \text{ on } \partial D\right\}. \tag{3.1}$$

We recall the definition of shape derivative [32].

Definition 3.1. *A shape functional $J(S)$ is shape differentiable at S if the map $\theta \in \Theta_{ad} \mapsto J((Id + \theta)(S))$ is Fréchet-differentiable at 0. The corresponding derivative $J'(S)$ is a continuous linear form on $W^{1,\infty}(D, \mathbb{R}^d)$ and satisfies*

$$J((Id + \theta)(S)) = J(S) + \langle J'(S), \theta\rangle + o(\theta), \ \textit{with} \ \lim_{\theta\to 0} \frac{|o(\theta)|}{\|\theta\|_{W^{1,\infty}}} = 0. \tag{3.2}$$

The shape derivative of volume and surface integrals of fixed functions is a classical result [8], [32].

Lemma 3.2. *Let $\mathcal{O}$ be a smooth bounded open set of $\mathbb{R}^d$ and $\theta \in W^{1,\infty}(\mathbb{R}^d, \mathbb{R}^d)$. Let $f \in H^1(\mathbb{R}^d)$ and $g \in H^2(\mathbb{R}^d)$ be two given functions. Assume that γ is a smooth subset of $\partial\mathcal{O}$ with boundary $\partial\gamma$. The shape derivatives of*

$$J_1(\mathcal{O}) = \int_{\mathcal{O}} f\,dx \quad \text{and} \quad J_2(\gamma) = \int_{\gamma} g\,ds$$

are given by

$$\langle J_1'(\mathcal{O}), \theta\rangle = \int_{\partial\mathcal{O}} f\,\theta\cdot\nu\;ds \tag{3.3}$$

and

$$\langle J_2'(\gamma), \theta\rangle = \int_{\gamma} \left(\frac{\partial g}{\partial \nu} + g\kappa\right)\theta\cdot\nu\;ds + \int_{\partial\gamma} g\,\theta\cdot\tau\;dl, \tag{3.4}$$

where ν is the unit exterior normal vector to $\partial\mathcal{O}$, κ is the mean curvature, τ is the unit tangent vector to $\partial\mathcal{O}$ such that τ is normal to both $\partial\gamma$ and ν, and dl is the $(d-2)$ dimensional measure along $\partial\gamma$.

Remark 3.3. *The result* (3.4) *is usually stated when $\gamma = \partial\mathcal{O}$ which has no $d-2$ dimensional boundary $\partial\gamma$. When γ has a boundary, the proof of* (3.4) *yields an additional term on $\partial\gamma$ which is due to an integration by parts on the surface γ (see [36]).*

3.2 Shape derivative computation

The goal is to compute the shape derivative of the objective function (2.10), which is the compliance for the variational problem (2.7). This choice of the objective function makes the problem self-adjoint and simplifies the computations. The originality of this computation is that the solution is discontinuous through the interface Γ because of the imperfect transmission condition on Γ.

To ease the computation we slightly change the notation for the compliance (2.10), which is rewritten as

$$J(S) = L(u_\omega, u_S, S),$$

where u_ω, respectively u_S, is the restriction of the solution u of (2.7) to ω, respectively S. The various loading cases lead to two different general forms of L.

- Given $F_1, F_2 \in H^1(D)^d$, $v_1, v_2 \in H^1(D)^d$, define

$$L(v_1, v_2, S) := \int_\omega F_1\cdot v_1\,dx + \int_S F_2\cdot v_2\,dx. \tag{3.5}$$

- Given $f_1, f_2 \in H^2(D)^d$, $v_1, v_2 \in H^2(D)^d$ and $C_1, C_2 \in \mathbb{R}$ such that $C_1 + C_2 = 1$, define

$$L(v_1, v_2, S) := \int_{\partial\omega\setminus\partial S} f_1\cdot v_1\,ds + \int_{\partial\omega\cap\partial S} f_2\cdot(C_1v_1 + C_2v_2)\,ds. \tag{3.6}$$

Proposition 3.4. *Under Assumption 2.1, the compliance* (2.10) *is shape differentiable and, for any $\theta \in \Theta_{ad}$, its shape derivative writes as*

(i) if L is given by (3.5),

$$\langle J'(S), \theta\rangle = \int_{\partial S\setminus\partial\omega} (-\sigma(u_S) : e(u_S) + 2F_2\cdot u_S)\;\theta\cdot n\,ds - \int_{\partial\Gamma} R^{-1}[u]\cdot[u]\theta\cdot\tau\,dl, \tag{3.7}$$

(ii) if L is given by (3.6),

$$\begin{aligned}\langle J'(S),\theta\rangle = &\int_{\partial S\setminus\partial\omega}(-\sigma(u_S):e(u_S))\,\theta\cdot n\,ds - \int_{\partial\Gamma} R^{-1}[u]\cdot[u]\,\theta\cdot\tau\,dl\\ &+\int_{\partial(\partial\omega\setminus\partial S)} 2f_1\cdot u_\omega\,\theta\cdot\tau\,dl + \int_{\partial\Gamma} 2f_2\cdot(C_1u_\omega + C_2u_S)\,\theta\cdot\tau\,dl,\end{aligned} \tag{3.8}$$

where u is the solution of (2.7), *σ is the stress tensor defined by* (2.6), *the jump $[\cdot]$ is defined in* (2.8) *as $[\varphi]=\varphi|_S-\varphi|_\omega$, $n=n_S$ and τ is the tangent vector which is orthogonal to the normal ν (see Figure 1).*

Proof. The shape derivatives are computed by means of Céa fast derivation method [16]. Introduce a general Lagrangian:

$$\mathcal{L}:\Theta_{ad}\times H^1_{\Gamma_D}(D)^d\times H^1_{\Gamma_D}(D)^d\times H^1_{\Gamma_D}(D)^d\times H^1_{\Gamma_D}(D)^d\to\mathbb{R}$$

$$\begin{aligned}\mathcal{L}(\theta,v_1,v_2,q_1,q_2) := L(v_1,v_2,(I+\theta)S) &+\sum_{i=1}^{2}\int_{(I+\theta)\mathcal{O}_i}\sigma(v_i):e(q_i)dx\\ &+\int_{(I+\theta)\Gamma} R^{-1}(v_2-v_1)(q_2-q_1)ds - L(q_1,q_2,(I+\theta)S),\end{aligned}$$

where $\mathcal{O}_1=\omega$ and $\mathcal{O}_2=S$. As usual, differentiating with respect to v_1,v_2 and imposing the optimality condition, lead to the adjoint problem which in this case (for both L under consideration) has the solution $p=-u$. Differentiating with respect to q_1,q_2 and imposing the optimality condition, yield the state equation given by the variational formulation (2.7). Because of (2.7), the Lagrangian simplifies when $(v_1,v_2)=(u_\omega,u_S)$ and, for any q_1,q_2, it yields

$$\mathcal{L}(\theta,u_\omega,u_S,q_1,q_2)=J((I+\theta)S).$$

Then, using the chain rule lemma and imposing the previous optimality conditions we deduce

$$\langle J'(S),\theta\rangle = \partial_\theta\mathcal{L}(0,u_\omega,u_S,p_\omega,p_S)(\theta),$$

where the right-hand side has to be computed by using (3.3) and (3.4) from Lemma 3.2 since the functions $u_\omega,u_S,p_\omega,p_S$ are fixed when differentiating with respect to θ. Recall that the adjoint is $p=-u$ and that $\theta\cdot n=0$ on $\partial\omega$ in view of (3.1).

(i) For (3.5) we obtain

$$\begin{aligned}\partial_\theta\mathcal{L}(0,u_\omega,u_S,p_\omega,p_S)(\theta) = &\int_{\partial S}(\theta\cdot n)F_2\cdot u_S\,ds + \int_{\partial S}(\theta\cdot n)\sigma(u_S):e(p_S)\,ds\\ &-\int_{\partial S}(\theta\cdot n)F_2\cdot p_S\,ds + \int_{\partial\Gamma}(\theta\cdot\tau)R^{-1}[u]\cdot[p]\,dl,\end{aligned}$$

where R^{-1} does not need to be differentiated since ν and τ do not depend on S (but on ω which is fixed). This yields the desired result (3.7).

(ii) For (3.6) we obtain

$$\begin{aligned}\partial_\theta\mathcal{L}(0,u_\omega,u_S,p_\omega,p_S)(\theta) = &\int_{\partial(\partial\omega\setminus\partial S)}(\theta\cdot\tau)f_1\cdot u_\omega\,dl + \int_{\partial(\partial\omega\cap\partial S)}(\theta\cdot\tau)f_2\cdot(C_1u_\omega+C_2u_S)\,dl\\ &-\int_{\partial(\partial\omega\setminus\partial S)}(\theta\cdot\tau)f_1\cdot p_\omega\,dl - \int_{\partial(\partial\omega\cap\partial S)}(\theta\cdot\tau)f_2\cdot(C_1p_\omega+C_2p_S)\,dl\\ &+\int_{\partial S}(\theta\cdot n)\sigma(u_S):e(p_S)\,ds + \int_{\partial\Gamma}(\theta\cdot\tau)R^{-1}[u]\cdot[p]\,dl,\end{aligned}$$

which leads to the desired result (3.8) since $p=-u$. □

Remark 3.5. *As pointed out in Remark 2.2, when $\alpha = 0$ and $\beta = 0$ we recover from Proposition 3.4 the formula for the perfect interface case (see [4]). As already said, Proposition 3.4 is valid only under the assumption that the shape ω remains fixed. If both ω and S are optimized simultaneously, additional terms appear in the shape derivative (see [4] for more details on this issue in the case of a perfect interface).*

Remark 3.6. *At first glance, Proposition 3.4 can furnish a descent direction for a gradient-based algorithm. For example, considering formula* (3.7) *a* naive *descent direction is*

$$\theta = (\sigma(u_S) : e(u_S) - 2F_2 \cdot u_S)n + R^{-1}[u] \cdot [u]\delta_{\partial\Gamma}\tau, \tag{3.9}$$

where $\delta_{\partial\Gamma}$ is the Dirac mass of the interface boundary. However, this choice is not suitable since the first term in (3.9) *is defined only on Γ and the second term is defined only on $\partial\Gamma$. It should be extended to the whole domain D for numerical purposes (see [8, Section 5.2.2]). Following a classical idea [10] we perform an* extension-regularization *of the shape derivative, by solving the variational problem*

$$\begin{cases} \text{Find } Q \in V := \left\{W \in H^1(D)^d : \ W \cdot n = 0 \text{ on } \partial D\right\} \text{ such that:} \\ \forall W \in V, \ a(Q, W) := \displaystyle\int_D \left(\gamma_{reg}^2 \nabla Q : \nabla W + Q \cdot W\right) dx = \langle J'(S), W\rangle \end{cases} \tag{3.10}$$

where the regularization parameter $\gamma_{reg} > 0$ is taken of the order of the minimal cell size from the mesh of D. Notice that this process is guaranteed to provide a descent direction $-Q$. Indeed, taking $W = -Q$, we have

$$\langle J'(S), -Q\rangle = -\int_D \left(\gamma_{reg}^2 \nabla Q : \nabla Q + |Q|^2\right) dx \leq 0.$$

Note that there are two delicate theoretical issues in using (3.10) *for computing a descent direction. First, it is not clear that the solution Q belongs to the space $W^{1,\infty}(D, \mathbb{R}^d)$ as required. Second, the second term in* (3.9) *gives rise to an integral on $\partial\Gamma$ for the right hand side of* (3.10) *and there is no such trace theorem for functions in the space $V \subset H^1(D)^d$. Nevertheless, it works perfectly fine in numerical practice and the interested reader is referred to [8, Section 5.2] for a detailed discussion.*

4 Numerical implementation

We explain how to solve the system (2.7) and to compute the shape derivatives (3.7) or (3.8) in numerical practice.

4.1 Resolution of direct problems

While in the case of perfect bonding, it is completely standard to solve (2.9) with Lagrange finite elements, it is not so obvious to solve (2.7) which features discontinuous functions through the interface. Nonetheless, there exist several methods to discretize the broken Sobolev space H^1_b. For example, one could rely on discontinuous Galerkin methods, extended finite element methods (XFEM, see e.g. [25]), unfitted finite elements [29], or immersed finite elements [35]. We propose yet a different approach which is easy to implement in a finite element software like FreeFem++ [31]. It is a penalization approach which amounts to extend the function u_ω and u_S, solely defined in ω or S respectively, to functions $u_\omega^\varepsilon, u_S^\varepsilon$ defined in the entire domain D. Here, $\varepsilon > 0$ is a small penalization

parameter (typically $\varepsilon = 10^{-6}$ for our computations) which is used to extend each function outside its original domain of definition. Denote by $\mathcal{O} \in \{S, \omega\}$ any of the two subdomains and introduce the following subspaces of $H^1(\Omega)^d$

$$V_{\mathcal{O}} := \left\{ v \in L^2(\Omega)^d \text{ such that } \nabla v \in L^2(\mathcal{O})^{d\times d},\ v = 0 \text{ on } \Gamma_D \right\}.$$

Functions in $V_{\mathcal{O}}$ are defined in the complete domain Ω but belong only to $H^1(\mathcal{O})^d$. The penalization of (2.7) is the following variational formulation: find $(u_\omega^\varepsilon, u_S^\varepsilon) \in V_\omega \times V_S$ such that for every $(v_\omega, v_S) \in V_\omega \times V_S$

$$\sum_{\mathcal{O}\in\{S,\omega\}} \left(\int_{\mathcal{O}} \sigma(u_{\mathcal{O}}^\varepsilon) : e(v_{\mathcal{O}}) dx - \int_{\mathcal{O}} F \cdot v_{\mathcal{O}} dx \right) + \int_\Gamma R^{-1}(u_S^\varepsilon - u_\omega^\varepsilon) \cdot (v_S - v_\omega) ds$$
$$+\varepsilon \left(\int_\omega u_S^\varepsilon \cdot v_S dx + \int_S u_\omega^\varepsilon \cdot v_\omega dx \right) = L(v_\omega, v_S), \tag{4.1}$$

The additional zero-order terms, penalized by $\varepsilon > 0$, make (4.1) well-posed, thanks to our choice of space $V_{\mathcal{O}}$. In particular, (4.1) admits a unique solution by applying the Lax-Milgram lemma. In practice, the finite element discretization of $V_{\mathcal{O}}$ can be the same as that of $H^1(\Omega)^d$. In the end, only the restrictions of u_ω^ε to ω and of u_S^ε to S are used.

As expected, when $\varepsilon \to 0$, the sequence $(u_\omega^\varepsilon, u_S^\varepsilon)$ converges in $H^1(\omega)^d \times H^1(S)^d$ to (u_ω, u_S), the unique solution in $\mathbf{X}_0$ of (2.7).

Proposition 4.1. *Let $u_\omega^\varepsilon, u_S^\varepsilon$ be the unique solution of (4.1). Define $u^\varepsilon = u_\omega^\varepsilon \chi_\omega + u_S^\varepsilon \chi_S \in \mathbf{X}_0$. Then, u^ε converges in $\mathbf{X}_0$ to u, the unique solution of (2.7). Furthermore, denoting $J_\varepsilon(S) = L(u^\varepsilon)$, we have*

$$\lim_{\varepsilon\to 0} J_\varepsilon(S) = J(S) \quad \textit{and} \quad \lim_{\varepsilon\to 0} \langle J_\varepsilon'(S), \theta\rangle = \langle J'(S), \theta\rangle$$

for any $\theta \in \Theta_{ad}$.

The proof is a direct adaptation to the elasticity setting of the proof for the conductivity equation (see [5]) and it is safely left to the reader.

Remark 4.2. *Because of the imperfect transmission conditions across the interface Γ, which leads to an integral term on Γ in (4.1), it is useful to work with an exactly meshed interface in the reference mesh. Furthermore, since the part ω is fixed during the optimization process this body-fitted mesh does not change during optimization. In practice, we use the meshing software* `mmg` *[17, 21] to build a mesh of the computational domain D such that its subdomain ω is also exactly meshed. One further advantage of the exact meshing of the interface is to avoid any further smoothing process for a diffused-interface model as in [6, 49].*

Although the part ω is exactly meshed, it is not the case of the support S, which is captured by a level set function in the domain $D \setminus \omega$ (see the next subsection). Therefore, we rely on the well-known ersatz material method, which consists in extending the integrals on S to $D \setminus \omega$ in (4.1) with a Hooke's law $A_\eta = \eta A_S$ in $D \setminus (\omega \cup S)$, where $\eta > 0$ is a small parameter (typically $\eta = 10^{-3}$) and A_S is the Hooke's law of the support S.

4.2 Level set method

The shape and topology optimization of the support S is performed with the level set method, introduced by Osher and Sethian [46]. We refer to [8] for details on its use in the context of structural optimization.

Recall that the support S does not intersect the part ω, which is fixed during the optimization process. Therefore, the support S can be represented by a level set function ϕ defined in the subdomain $D \setminus \omega$ by

$$\begin{cases} \phi(x) < 0 \Leftrightarrow x \in S \\ \phi(x) = 0 \Leftrightarrow x \in \partial S \\ \phi(x) > 0 \Leftrightarrow x \in (D \setminus \omega) \setminus S. \end{cases}$$

In order to avoid any interpolation or projection techniques between the finite element fields and the level set function, we use the same mesh for both quantities. Since $D \setminus \omega$ is exactly meshed, it is a simplicial mesh and not a cartesian one. Therefore, we cannot rely on finite difference algorithms to solve the Hamilton-Jacobi equation giving the evolution of ϕ. Rather, we use a linearization of the Hamilton-Jacobi equation

$$\partial_t \phi + \theta \cdot \nabla \phi = 0 \quad \text{ on } [0, \tau] \times D \setminus \omega, \tag{4.2}$$

where the velocity $\theta(x)$ is given by the extension-regularization procedure for the shape derivative discussed in Remark 3.6. The transport equation (4.2) is solved with the method of characteristics, implemented in the open source software `advect` (see [14] for more details).

4.3 Lagrangian optimization algorithm

To minimize the objective function $J(S)$ with a volume constraint on S, one simple algorithm is to introduce a Lagrangian

$$\mathcal{L}(S, \lambda) := J(S) + \lambda \left(\int_S dx - V_{sup} \right),$$

where λ is a Lagrange multiplier, and to find its saddle point. More precisely, the Lagrangian is minimized with respect to S and the Lagrange multiplier is updated during the optimization process in order to satisfy the constraint at convergence. This Lagrangian algorihtm is simple to implement, but its convergence is rather slow.

Therefore, we rather use an Augmented Lagrangian algorithm [45] which is more efficient. To impose an equality constraint $c(S) = 0$, we consider the augmented Lagrangian

$$\mathcal{L}(S, \lambda, \mu) := J(S) - \lambda c(S) + \frac{\mu}{2} c^2(S),$$

where λ is expected to converge to the Lagrange multiplier of the constraint and $\mu > 0$ is a penalty parameter. The multiplier is updated using

$$\lambda^{k+1} = \lambda^k - \mu^k c(S^k), \tag{4.3}$$

as shown in [45]. It is classical that for the Augmented Lagrangian algorithm it is not necessary to take a sequence of $\mu^k \to +\infty$. Here, μ^k is increased every 5 iterations:

$$\mu^k = \begin{cases} C\mu^{k-1} & \text{if } k \text{ is a multiple of 5,} \\ \mu^{k-1} & \text{if not,} \end{cases} \tag{4.4}$$

with $C > 1$ (we take $C = 1.1$), which helps to enforce the constraint along iterations. At each iteration the current support S^k is advected to a new support S^*, by solving the level set equation (4.2). In order to accept this iteration, we check that:

$$\mathcal{L}(S^*, \lambda^k, \mu^k) \leq \mathcal{L}(S^k, \lambda^k, \mu^k) + \text{tol} \, |\mathcal{L}(S^k, \lambda^k, \mu^k)|, \tag{4.5}$$

where tol is a tolerance level which is initialized with value tol $= 0.05$ and is gradually reduced along iterations, in order to avoid big oscillations, until tol $= 0.001$. If condition (4.5) is satisfied, we set $S^{k+1} = S^*$ and we update the Lagrangian parameters with (4.3) and (4.4). Note that the final time τ for the level set equation (4.2) is proportional to a descent step, which is also adapted at each iteration (its initial value is typically $\text{step}_{init} = 1$, while its minimal value is $\text{step}_{min} = 0.05\text{step}_{init}$)

$$\tau^k = \text{step}^k \frac{h}{\|\theta^k\|_\infty + 1e-6},$$

where h is the typical size of a cell in the mesh. The general algorithm used in our simulations is described in Algorithm 1.

Algorithm 1 Support optimization by a level set method

Require: S^0 and ϕ^0.
  Initialize step $= \text{step}_{init}$.
  while $k \leq k_{maxiter}$ **do**
    Solve the direct problem (4.1) with the support S^k.
    Compute the advection velocity θ^k solution of (3.10).
    Define $\tau = \text{step}\, h/(\|\theta^k\|_\infty + 1e-6)$.
    Solve (4.2) with $\phi(0) = \phi^k$ and $\theta = -\theta^k$. Define $\phi^* = \phi(\tau)$.
    Define the new support $S^* := \{x \in D \setminus \omega :\ \phi^*(x) < 0\}$.
    if (4.5) is verified **then**
      $S^k \leftarrow S^*$, $\phi^k \leftarrow \phi^*$, step $\leftarrow 1.2$step
      Update Lagrangian parameters by (4.3) and (4.4).
      break
    else
      No replacement of ϕ^k and S^k, step $\leftarrow \max(0.5\text{step}, \text{step}_{min})$.
    end if
    $k \leftarrow k + 1$
  end while

5 Numerical Examples

All simulations were performed in a sequential mode on a personal laptop with an `Intel i7 8th-gen processor` and 16 GB of RAM. The finite element analysis is performed with the `FreeFEM++` software [31]. The level set algorithm uses the advection routine `advect` [14] from the `ISCDtoolbox` and its re-initialization as a signed distance function is done with `mshdist` [18] also from the `ISCDtoolbox`. For the examples where the built shape is first obtained from a compliance minimization, or when the geometric definition of the part is too complex to be explicitely constructed (e.g. Cantilever and Bridge examples for the first case, 3-d table for the second one), we use the software `mmg` [17, 21] to obtain a perfectly meshed interface. All presented figures were obtained via post-processing using `Paraview`. We systematically make comparisons of the optimized supports obtained with our imperfect interface model with the ones obtained with a classical perfect interface (in such a case the algorithmic implementation is exactly the same). In all examples the mechanical parameters are set to

$$E_S = E_\omega = 1.0,\ \nu_S = \nu_\omega = 0.3,\ \lambda_S = \lambda_\omega = \nu\frac{E}{(1+\nu)(1-2\nu)},\ \mu_S = \mu_\omega = \frac{E}{2(1+\nu)}.$$

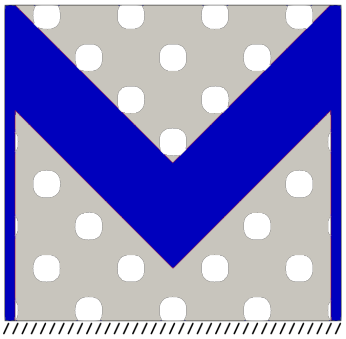

Figure 2: The M-shape ω (in blue) and the initialization for the support S (in grey).

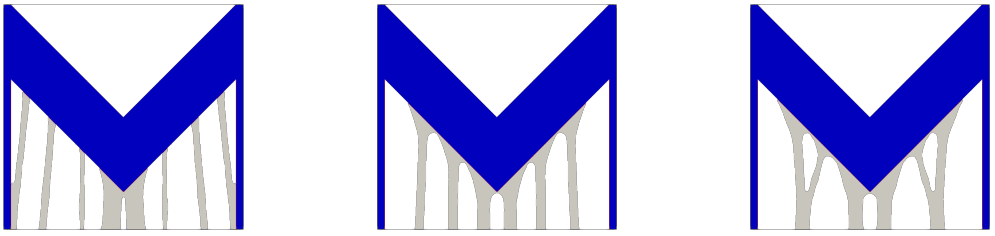

Figure 3: Optimized designs for $\alpha = \beta = 0.001$ (left), $\alpha = \beta = 20$ (center) and $\alpha = \beta = 50$ (right).

However, the optimization algorithm can also be applied to more realistic values and different material properties for the supports and the built part.

5.1 Example 1: 2-d structures under their own weight

In this subsection supports are optimized so that the compliance of the supported structure is minimal under the sole weight of the built part (see Subsection 2.2). In this case we consider the shape derivative given by (3.7) with $F_\omega = \rho_\omega g$ with $g = (0, -1)$, $\rho_\omega = 1$ and $F_S = 0$.

5.1.1 M structure

In this example the part ω is the M-shape represented in Figure 2. The supports and the part are attached to the baseplate and the rest of the boundary has a traction free boundary condition. The target volume for supports is $V_{sup} = 1.0$ and the bounding box is $D = [-1.6, 1.6]^2$. For this example the mesh has 28,510 vertices. The optimized designs, obtained from the initialization in Figure 2, are displayed in Figures 3, 4 and 5 for various values on the interface compliance parameters α, β. The smallest values $\alpha = \beta = 0.001$ correspond to the perfect interface setting (these values give exactly the same results as the classical transmission condition through the interface).

A first observation is that, as α, β increase (and therefore the interface becomes weaker), the thickness of the individual supports increase, as well as the contact area between the part and the supports. In Figures 4 and 5 one can see that, whenever the interface gets weaker in some direction (tangential if α increases, normal if β increases), the supports begin to align with the stronger direction. This is even more obvious for the larger differ-

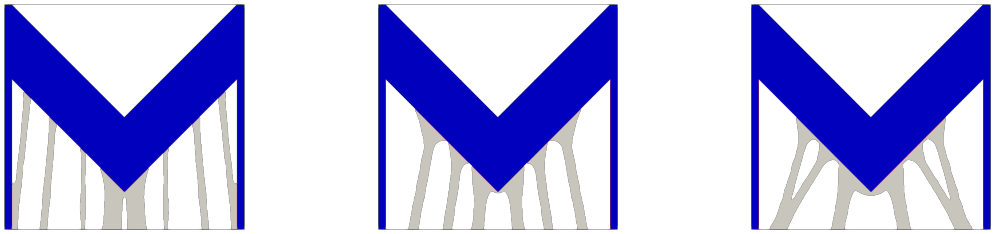

Figure 4: Tangentially weak case: optimized designs for $\alpha = \beta = 0.001$ (left), $\alpha = 20, \beta = 10$ (center) and $\alpha = 50, \beta = 10$ (right).

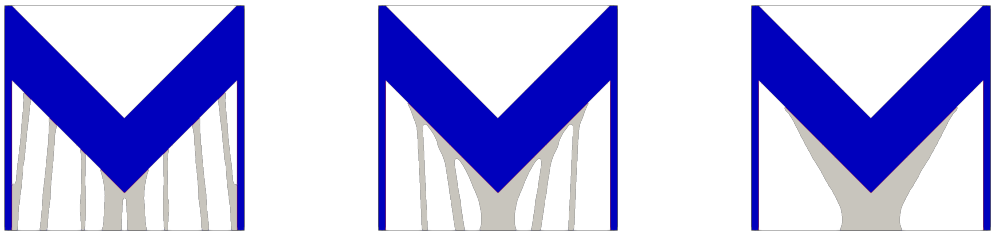

Figure 5: Normally weak case: optimized designs for $\alpha = \beta = 0.001$ (left), $\alpha = 10, \beta = 20$ (center) and $\alpha = 10, \beta = 50$ (right).

ences between α and β. Note that the lower corner of the M is more and more supported, as the interface gets weaker, especially in the normally weak case. A typical convergence history is shown in Figure 6: they all behave similarly for other values of α, β.

5.1.2 Triangle structure

In this example the part ω is an equilateral triangle with side length 1.5, shown in Figure 7, which has a volume $V_{part} = 9\sqrt{3}/16 \approx 0.974$. The computational domain is the square $D = [-1.5, 1.5]^2$. The target volume for the supports is $V_{sup} = 1.0$. Supports can attach to the bottom and lateral sides of D. For this example the mesh has 26,465 vertices. Results are shown in Figure 8.

On this example, the change in the topology of supports is even more dramatic when the interface gets weaker. For the perfect interface, the optimized support is a big vertical pillar (see Figure 8 upper left), while for the two weak interfaces on the right side, the supports are much more complex, taking advantage of the lateral walls. It is only for the normally-weak interface that the optimized support is again a single vertical pillar because of the very large tangential contact area with the lower side of the triangle (see Figure 8 lower left).

5.1.3 Cantilever

In this example the part ω is the cantilever shown in Figure 9, which has a volume $V_{part} = 0.8$. The computational domain is $D = [0, 2] \times [0, 1]$. The target volume for the support S is $V_{sup} = 0.25$. The supports and the part are attached to the baseplate (the lower side of D). For this example the mesh has 22,342 vertices. Results are displayed on Figure 10.

For a perfect interface, the optimized supports are mostly vertical bars (see Figure 10 upper left). For the various imperfect cases there is again an increase of the contact

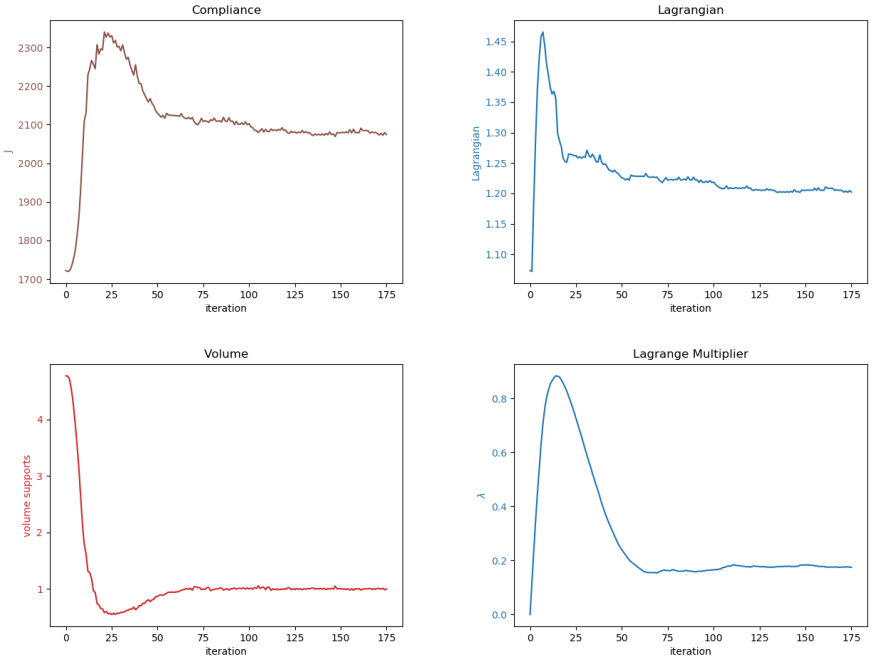

Figure 6: Convergence history for the case $\alpha = \beta = 50$.

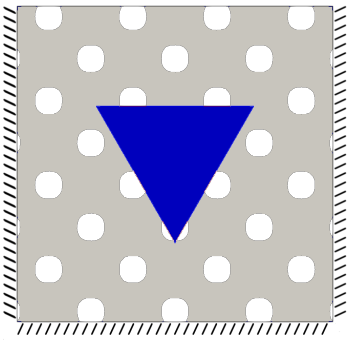

Figure 7: Triangle-shape ω (in blue) and the initialization for the support S (in grey).

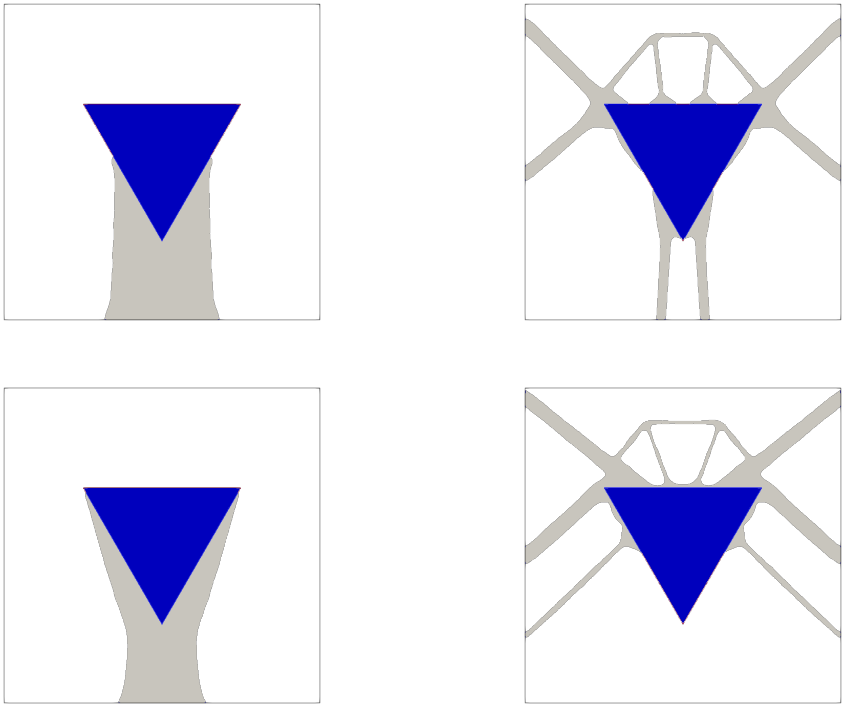

Figure 8: Optimized designs for $\alpha = \beta = 0.001$ (upper left), $\alpha = \beta = 50$ (upper right), $\alpha = 10, \beta = 50$ (lower left) and $\alpha = 50, \beta = 10$ (lower right).

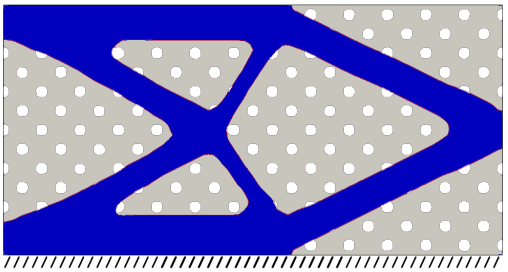

Figure 9: Cantilever-shape ω (in blue) and the initialization for the support S (in grey).

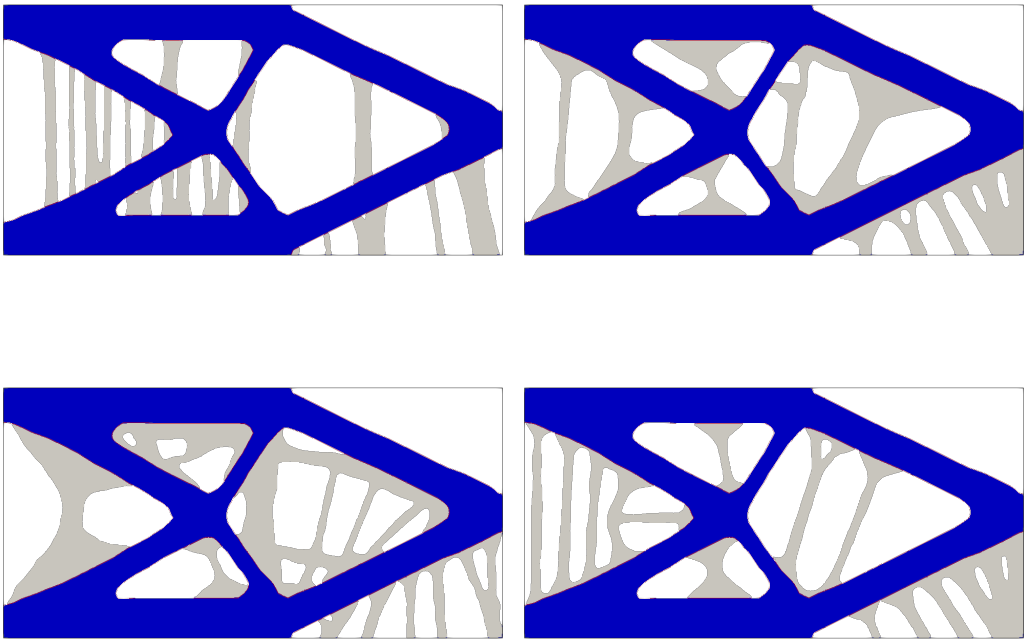

Figure 10: Optimized designs for $\alpha = \beta = 0.001$ (upper left), $\alpha = \beta = 50$ (upper right), $\alpha = 10, \beta = 50$ (lower left) and $\alpha = 50, \beta = 10$ (lower right).

area between the part and its supports. There is also an alignment (less obvious but still noticeable) of the supports with the strongest direction of the interface (normally weak: Figure 10 lower left ; tangentially weak: Figure 10 lower right).

5.1.4 Bridge

This bridge example is a classical engineering problem. The computational domain for half of the bridge is $D = [0, 2]^2$ and it is symmetrized with respect to the vertical axis. As a preliminary step a simple compliance minimization is performed (without any support) in order to obtain the bridge shape. The optimized bridge is shown on the right of Figure 11, obtained from the initialization on the left (notice the non-optimizable region in dark-blue where a vertical unitary force is applied along its upper boundary, the optimizable region is depicted in light-blue). This optimized bridge is used, in a second step, as the fixed part ω for which supports S are optimized. The volume of the bridge is $V_{part} = 0.8$, while the target volume for supports is $V_{sup} = 0.7$. The supports and the part are attached to the baseplate. For this example the mesh has 43407 vertices. Results are presented in Figure 12.

When the imperfection increases we can notice a higher contact surface and the appearance of a support structure above the bridge which somehow coincides with the lack of internal support bars (see Figure 12),

5.2 Example 2: 2-d structure under a thermoelastic force

In this subsection supports are optimized for a part subjected to a thermoelastic equivalent force, which is due to thermal gradients produced during the fabrication process. This

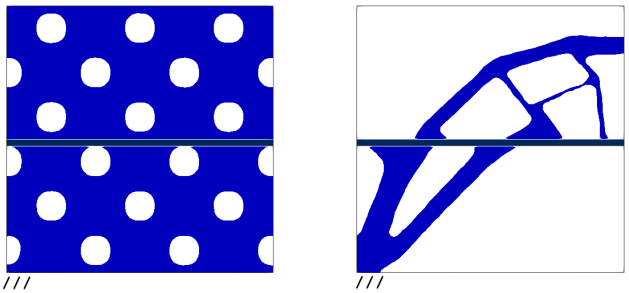

Figure 11: Initialization and Optimized design (compliance minimization): Bridge shape.

model is described in Subsection 2.3 and the optimization algorithm relies on formula (3.8) of the shape derivative. In our case, we have considered a synthetic force f_{th}, given by an algebraic expression, calibrated in order to replicate a perfect interface support optimization presented in [3]. We provide the construction of this force, as well as the construction of the mesh used in this example in the supplementary material. Here the part ω is half of a plane table, shown in Figure 13, and a symmetry condition is applied to the vertical left boundary of the square $D = [0, 1]^2$. The volume of the half table is $V_{part} = 0.12$, while the target volume for the support is $V_{sup} = 0.15$. The supports and the part are attached to the baseplate. For this example the mesh has 19,510 vertices. The thermoelastic equivalent force f_{th} is depicted in Figure 13.

In a first test, the thermoelastic force f_{th} is assumed to apply only on the part. In other words the right hand side of the variational formulation (4.1) is given by (2.11), namely $L(v) = \int_{\partial\omega} f_{th} \cdot v_\omega \, ds$. Results are shown in Figure 14. Again, it can be observed that supports are oriented differently according to the strongest direction of the interface rigidity. But, more surprisingly, the weakness of the interface makes it advantageous to put supports *above* the table and not only below it. This is one more manifestation of the strong influence of the interface model on the design of optimal supports. Of course, in a practical AM layer by layer process, the table would be finished before the upper part of the support is build and thus it is not helpful at all. This is due to our mechanical model which considers the complete supported structure at once. This defect of the model can easily be corrected by using a layer by layer model, as proposed in [7, 9], at the price of a serious increase in the required CPU time.

In a second test, the thermoelastic force is applied on both sides of the interface Γ and the right hand side of the variational formulation (4.1) is given by (2.12), namely $L(v) = \int_{\partial\omega\setminus\partial S} f_{th} \cdot v_\omega \; ds + \int_{\partial\omega\cap\partial S} f_{th} \cdot (v_\omega + v_S)/2 \, ds$. With the same optimization parameters we obtain the results in Figure 15. In most cases, the optimized supports are very similar to those presented in Figure 14. Changes concern the thickness of supports attached to the baseplate. The contact zones between part and support are also different. Notably, in the extreme case $\alpha = 1, \beta = 20$ (Figure 15 lower left) the second force model reduces the contact between the part and its support, compared to the first force model.

5.3 Example 3: 3-d structure under its own weight

In this subsection supports are optimized so that the compliance of the supported structure is minimal under the sole weight of the built part (see Subsection 2.2). In this case we consider the shape derivative given by (3.7) with $F_\omega = \rho_\omega g$ with $g = (0, 0, -1)$, $\rho_\omega = 1$ and

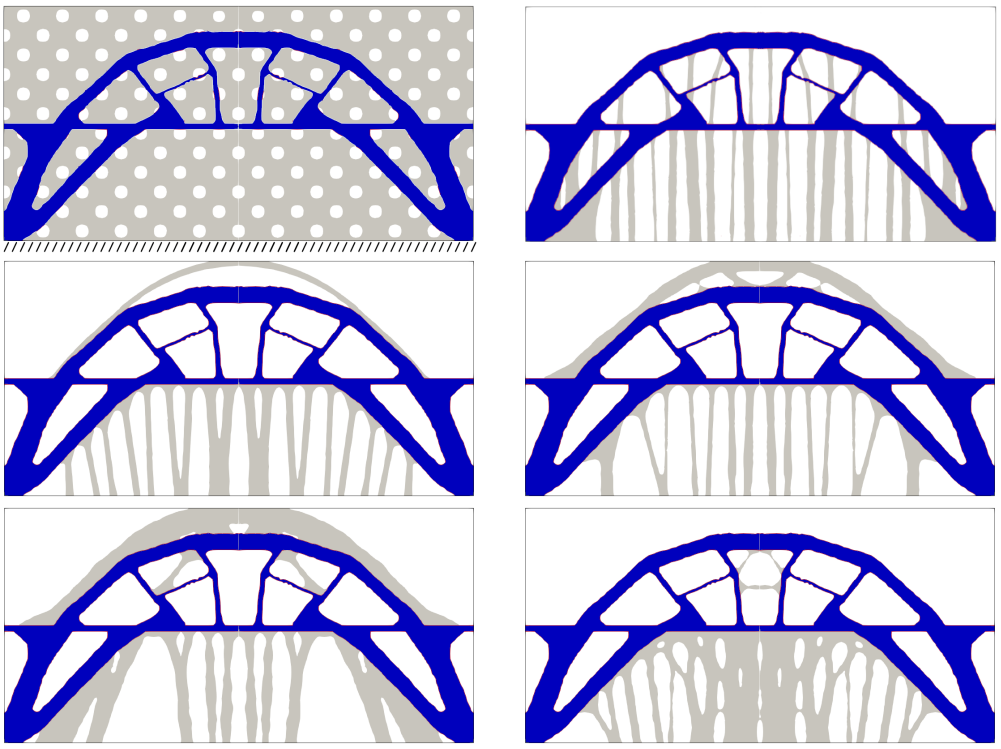

Figure 12: Support designs for the bridge: initialization and optimized design for a perfect interface (top row), optimized designs for $\alpha = \beta = 20$ and $\alpha = \beta = 50$ (middle row), optimized designs for $\alpha = 10, \beta = 50$ and $\alpha = 50, \beta = 10$ (lower row).

$F_S = 0$. Here the part ω is a quarter of a 3-d table (see Figure 16 left) which is extended by symmetry (see Figure 16 right). The computational domain is $D = [0,1]^3$, for 1/4 of the complete table. The volume of the table is $V_{part} = 0.06$, while the target volume of the support is $V_{sup} = 0.1$. The supports and the part are attached to the baseplate. For this example the mesh has 47,737 vertices.

In the perfect case (Figure 17 top row) a support made by vertical pillars is obtained. An extremely weak interface (Figure 17 2nd row) gives a support made by a few pillars and an additional arch holding the table from above with an increased contact zone. A tangentially-weak interface (Figure 17 3rd row) produces a support structure which resembles the perfect case with a slightly increased contact zone. This is because the original pillars of the support were already normal to the horizontal part of the table. Finally, when a normally-weak interface is considered (Figure 17 bottom row), the optimized support is no longer normal to the table but inclined, connected to the perimeter of the table, with an additional thin layer increasing the contact surface below.

6 Conclusions and perspectives

In this article we propose an algorithm for shape and topology optimization of supports which are imperfectly connected to the part, built by additive manufacturing techniques. Our numerical results prove that the design of supports is dramatically impacted by the type of interface conditions between part and support. In particular, the optimized supports may be very different in the perfect or imperfect interface case and they can also

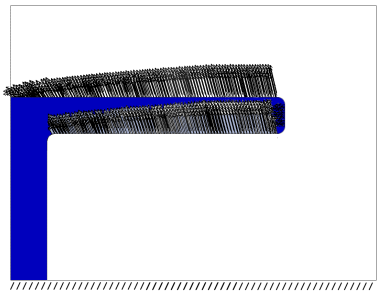

Figure 13: Thermoelastic equivalent force f_{th} for the half-table.

depend on the anisotropic rigidity of the interface. It is therefore crucial to take into account such an interfacial model in order to design truly optimal supports. Of course, the present work is just a first step in this direction and in particular our spring-like interfacial model can definitely be improved.

Many perspectives can be proposed for this work. The imperfect interface model considered here, being linear, treats equally compression and traction and therefore interpenetration can occur at the interface between part and support. A first possibility is thus to make the model non-linear and able to distinguish between compression and traction, like a contact model or like a Baremblatt cohesive-zone model [11]. Of course, other objective functions (on top of the compliance used here) and various additional constraints (like a penalization of the contact area as in [3]) could be considered, at the price of a slightly more involved and costly optimization algorithm. Likewise, the simultaneous optimization of part and supports, as in [4], could be done for the proposed imperfect interface model.

However, a key improvement is rather the replacement of the *all-in-one* mechanical model (2.7) by a physically more relevant *layer-by-layer* model, as already proposed in [7, 9], but at the price of a serious increase in the required computational time. Indeed, one surprising feature of some of our optimized supports is that they hold the built part from above, which is problematic when considering the layer by layer building process (the part would be finished before the above supports have played their role). This is due to the fact that the mechanical model (2.7) takes into account only the completely finished supported structure and not all the intermediate structures. Therefore, using a mechanical model based on all intermediate shapes would correct this default.

Finally, the imperfect interface model (2.8) relies on constitutive parameters α, β which represents the inverse of tangential and normal rigidities on the interface. They are not intrinsic material parameters but rather homogenized properties, modeling the macroscopic behavior of an interface with many microscopic details (holes, indentations, tree-like branching) which are not explicitly represented. Therefore, these parameters should be calibrated by using experimental data coming from real additive manufacturing experiments.

Replication of results

It is possible to implement Algorithm 1 using the free softwares listed in Section 5, which were used with the following versions:

- `FreeFem++`: v4.8. `http://www.freefem.org`
- `Advect`: 3.0a. `https://github.com/ISCDtoolbox/Advection`
- `mshdist`: 1.1b. `https://github.com/ISCDtoolbox/Mshdist`
- `mmg`: 5.4.3 (2-d), 5.5.2 (3-d). `http://www.mmgtools.org`
- `paraview`: 5.8.1. `http://www.paraview.org`

Furthermore, some of the meshes of our examples are provided at the following URL:

`https://sites.google.com/view/matiasgodoyc/research/supplementary-material`

Conflict of interest

On behalf of all authors, the corresponding author states that there is no conflict of interest.

Acknowledgements

This work was supported by the SOFIA project, funded by the BPI (Banque Publique d'Investissement).

References

[1] J. Aboudi. Damage in composites - modeling of imperfect bonding. *Composites Science and Technology*, 28(2):103–128, 1987.

[2] G. Allaire. *Conception optimale de structures*, volume 58 of *Mathématiques & Applications (Berlin) [Mathematics & Applications]*. Springer-Verlag, Berlin, 2007.

[3] G. Allaire, M. Bihr, and B. Bogosel. Support optimization in additive manufacturing for geometric and thermo-mechanical constraints. *Structural and Multidisciplinary Optimization*, 61(6):2377–2399, 2020.

[4] G. Allaire and B. Bogosel. Optimizing supports for additive manufacturing. *Struct. Multidiscip. Optim.*, 58(6):2493–2515, 2018.

[5] G. Allaire, B. Bogosel, and M. Godoy. Shape Optimization of an Imperfect Interface: Steady-State Heat Diffusion. *J. Optim. Theory Appl.*, 191(1):169–201, 2021.

[6] G. Allaire, C. Dapogny, G. Delgado, and G. Michailidis. Multi-phase structural optimization *via* a level set method. *ESAIM Control Optim. Calc. Var.*, 20(2):576–611, 2014.

[7] G. Allaire, C. Dapogny, R. Estevez, A. Faure, and G. Michailidis. Structural optimization under overhang constraints imposed by additive manufacturing technologies. *J. Comput. Phys.*, 351:295–328, 2017.

[8] G. Allaire, C. Dapogny, and F. Jouve. Shape and topology optimization. In A. Bonito and R. H. Nochetto, editors, *Geometric Partial Differential Equations - Part II*, volume 22 of *Handbook of Numerical Analysis*. Elsevier, 2021.

[9] G. Allaire and L. Jakabčin. Taking into account thermal residual stresses in topology optimization of structures built by additive manufacturing. *Mathematical Models and Methods in Applied Sciences*, 28(12):2313–2366, 2018.

[10] G. Allaire, F. Jouve, and A.-M. Toader. A level-set method for shape optimization. *C. R. Math. Acad. Sci. Paris*, 334(12):1125–1130, 2002.

[11] G. Barenblatt. The mathematical theory of equilibrium cracks in brittle fracture. volume 7 of *Advances in Applied Mechanics*, pages 55–129. Elsevier, 1962.

[12] C. Barlier and A. Bernard. *Fabrication additive - Du Prototypage Rapide à l'impression 3D*. Dunod, Paris, 2016.

[13] K. Bartsch, F. Lange, M. Gralow, and C. Emmelmann. Novel approach to optimized support structures in laser beam melting by combining process simulation with topology optimization. *J. of Laser Applications*, 31:022302, 2019.

[14] C. Bui, C. Dapogny, and P. Frey. An accurate anisotropic adaptation method for solving the level set advection equation. *Internat. J. Numer. Methods Fluids*, 70(7):899–922, 2012.

[15] F. Calignano. Design optimization of supports for overhanging structures in aluminum and titanium alloys by selective laser melting. *Materials & Design*, 64:203–213, 2014.

[16] J. Céa. Conception optimale ou identification de formes: calcul rapide de la dérivée directionnelle de la fonction coût. *RAIRO Modél. Math. Anal. Numér.*, 20(3):371–402, 1986.

[17] C. Dapogny, C. Dobrzynski, and P. Frey. Three-dimensional adaptive domain remeshing, implicit domain meshing, and applications to free and moving boundary problems. *J. Comput. Phys.*, 262:358–378, 2014.

[18] C. Dapogny and P. Frey. Computation of the signed distance function to a discrete contour on adapted triangulation. *Calcolo*, 49(3):193–219, 2012.

[19] M. C. Delfour and J.-P. Zolésio. *Shapes and geometries*, volume 22 of *Advances in Design and Control*. Society for Industrial and Applied Mathematics (SIAM), Philadelphia, PA, second edition, 2011.

[20] D. A. Di Pietro and A. Ern. *Mathematical aspects of discontinuous Galerkin methods*, volume 69 of *Mathématiques & Applications (Berlin) [Mathematics & Applications]*. Springer, Heidelberg, 2012.

[21] C. Dobrzynski and P. Frey. Anisotropic delaunay mesh adaptation for unsteady simulations. In *Proceedings of the 17th international Meshing Roundtable*, pages 177–194. Springer, 2008.

[22] V. Dolejší and M. Feistauer. *Discontinuous Galerkin method*, volume 48 of *Springer Series in Computational Mathematics*. Springer, Cham, 2015.

[23] J. Dumas, J. Hergel, and S. Lefebvre. Bridging the gap: Automated steady scaffoldings for 3d printing. *ACM Transactions on Graphics (TOG)*, 33(4):1–10, 2014.

[24] J. Dumas, J. Hergel, and S. Lefebvre. Bridging the gap: Automated steady scaffoldings for 3d printing. *ACM Trans. Graph.*, 33(4):98:1–98:10, July 2014.

[25] P. Duysinx, L. Van Miegroet, T. Jacobs, and C. Fleury. Generalized shape optimization using x-fem and level set methods. In *IUTAM Symposium on Topological Design Optimization of Structures, Machines and Materials*, pages 23–32. Springer, 2006.

[26] M. Gan and C. Wong. Practical support structures for selective laser melting. *Journal of Materials Processing Technology*, 238:474 – 484, 2016.

[27] N. Gardan and A. Schneider. Topological optimization of internal patterns and support in additive manufacturing. *Journal of Manufacturing Systems*, 37:417–425, 2015.

[28] I. Gibson, D. Rosen, and B. Stucker. *Additive Manufacturing Technologies*. Springer New York, 2015.

[29] A. Hansbo and P. Hansbo. An unfitted finite element method, based on Nitsche's method, for elliptic interface problems. *Comput. Methods Appl. Mech. Engrg.*, 191(47-48):5537–5552, 2002.

[30] A. Hansbo and P. Hansbo. A finite element method for the simulation of strong and weak discontinuities in solid mechanics. *Computer methods in applied mechanics and engineering*, 193(33-35):3523–3540, 2004.

[31] F. Hecht. New development in freefem++. *J. Numer. Math.*, 20(3-4):251–265, 2012.

[32] A. Henrot and M. Pierre. *Shape variation and optimization. A geometrical analysis*, volume 28. Zürich: European Mathematical Society (EMS), 2018.

[33] X. Huang, C. Ye, S. Wu, K. Guo, and J. Mo. Sloping wall structure support generation for fused deposition modeling. *The International Journal of Advanced Manufacturing Technology*, 42(11):1074–1081, 2009.

[34] A. Hussein, L. Hao, C. Yan, R. Everson, and P. Young. Advanced lattice support structures for metal additive manufacturing. *Journal of Materials Processing Technology*, 213(7):1019–1026, 2013.

[35] D. Kyeong and D. Y. Kwak. An immersed finite element method for the elasticity problems with displacement jump. *Adv. Appl. Math. Mech.*, 9(2):407–428, 2017.

[36] S. Lang. *Fundamentals of differential geometry*, volume 191 of *Graduate Texts in Mathematics*. Springer-Verlag, New York, 1999.

[37] M. Langelaar. Topology optimization of 3d self-supporting structures for additive manufacturing. *Additive Manufacturing*, 12:60–70, 2016.

[38] M. Langelaar. Combined optimization of part topology, support structure layout and build orientation for additive manufacturing. *Structural and Multidisciplinary Optimization*, 57(5):1985–2004, 2018.

[39] D. Leguillon and E. Sánchez-Palencia. *Computation of singular solutions in elliptic problems and elasticity*. John Wiley & Sons, Ltd., Chichester; Masson, Paris, 1987.

[40] R. Lipton. Effect of interfacial bonding on fiber reinforced shafts subject to antiplane shear. *Internat. J. Solids Structures*, 38(2):369–387 (2001), 2000.

[41] R. Lipton. Reinforcement of elastic structures in the presence of imperfect bonding. *Quart. Appl. Math.*, 59(2):353–364, 2001.

[42] R. Lipton and B. Vernescu. Composites with imperfect interface. *Proc. Roy. Soc. London Ser. A*, 452(1945):329–358, 1996.

[43] F. Mezzadri, V. Bouriakov, and X. Qian. Topology optimization of self-supporting support structures for additive manufacturing. *Additive Manufacturing*, 21:666–682, may 2018.

[44] A. M. Mirzendehdel and K. Suresh. Support structure constrained topology optimization for additive manufacturing. *Computer-Aided Design*, 81:1–13, 2016.

[45] J. Nocedal and S. J. Wright. *Numerical optimization*. Springer Series in Operations Research and Financial Engineering. Springer, New York, second edition, 2006.

[46] S. Osher and J. A. Sethian. Fronts propagating with curvature-dependent speed: algorithms based on Hamilton-Jacobi formulations. *J. Comput. Phys.*, 79(1):12–49, 1988.

[47] G. Strano, L. Hao, R. Everson, and K. Evans. A new approach to the design and optimisation of support structures in additive manufacturing. *The International Journal of Advanced Manufacturing Technology*, 66(9-12):1247–1254, 2013.

[48] J. Vanek, J. A. G. Galicia, and B. Benes. Clever support: Efficient support structure generation for digital fabrication. In *Computer graphics forum*, volume 33, pages 117–125. Wiley Online Library, 2014.

[49] N. Vermaak, G. Michailidis, G. Parry, R. Estevez, G. Allaire, and Y. Bréchet. Material interface effects on the topology optimization of multi-phase structures using a level set method. *Struct. Multidiscip. Optim.*, 50(4):623–644, 2014.

[50] Z. Zhong and S. Meguid. On the imperfectly bonded spherical inclusion problem. *J. Appl. Mech*, 66(4):839–846, 1999.

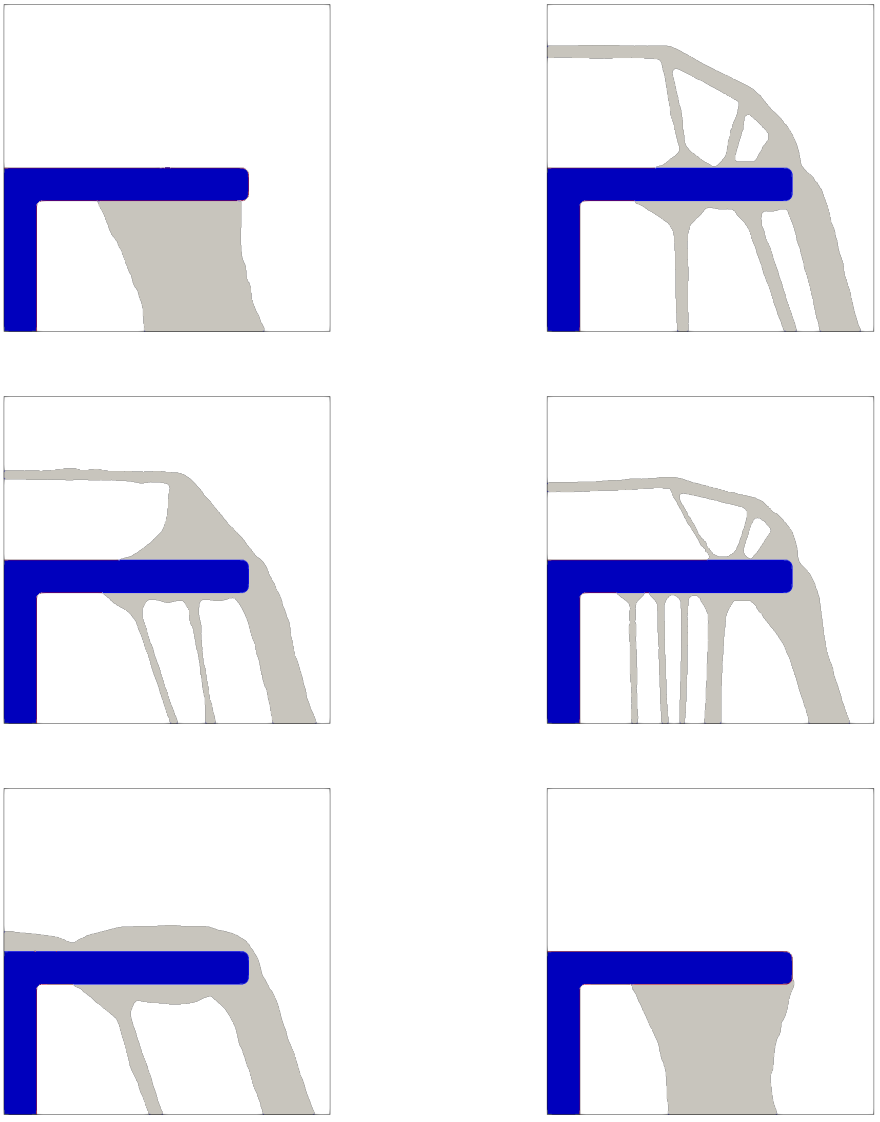

Figure 14: Optimized designs for the thermoelastic force f_{th} applied only to ω: $\alpha = \beta = 0.001$ (upper left), $\alpha = \beta = 50$ (upper right), $\alpha = 10, \beta = 50$ (middle left), $\alpha = 50, \beta = 10$ (middle right), $\alpha = 1, \beta = 20$ (lower left), $\alpha = 20, \beta = 1$ (lower right).

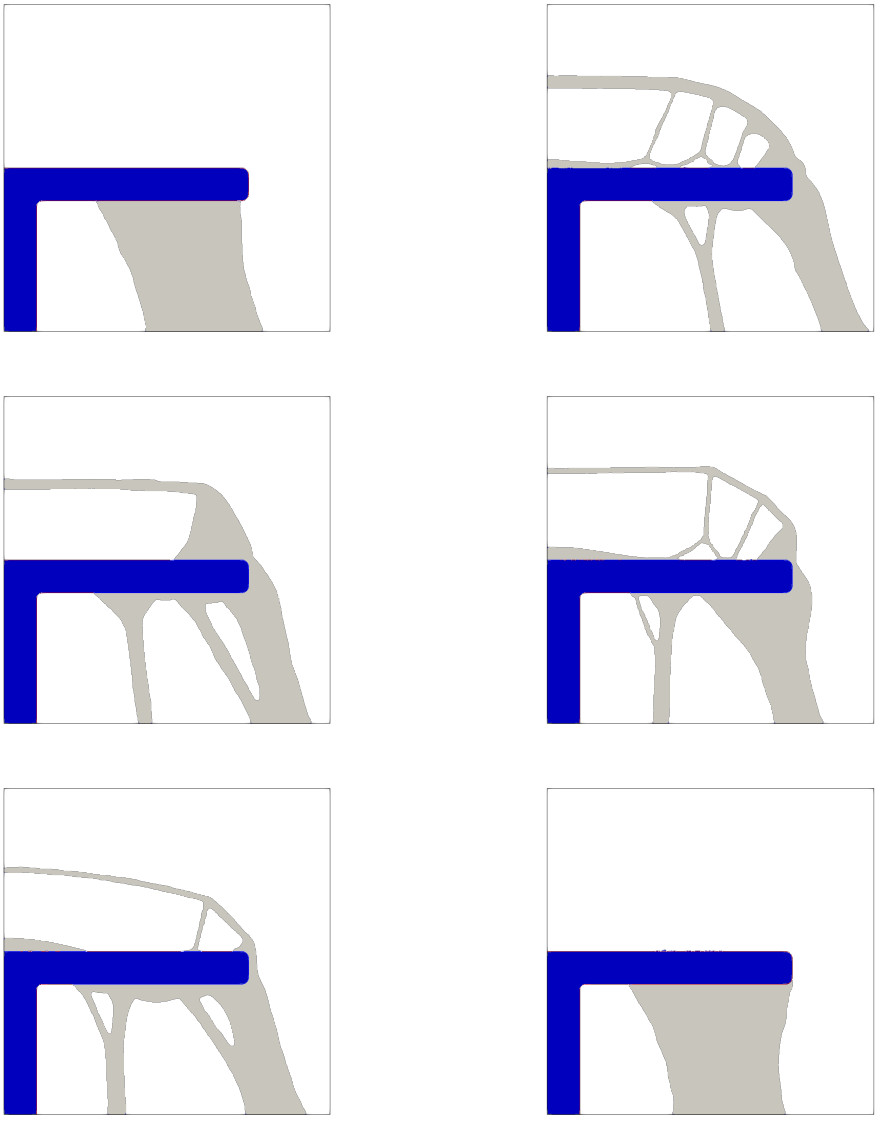

Figure 15: Optimized designs for the thermoelastic force f_{th} applied equally to ω and S: $\alpha = \beta = 0.001$ (upper left), $\alpha = \beta = 50$ (upper right), $\alpha = 10, \beta = 50$ (middle left), $\alpha = 50, \beta = 10$ (middle right), $\alpha = 1, \beta = 20$ (lower left), $\alpha = 20, \beta = 1$ (lower right).

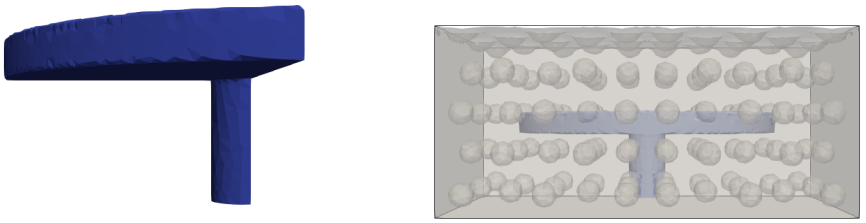

Figure 16: The 3-d table (in blue) and the support initialization (in grey) with holes inside.

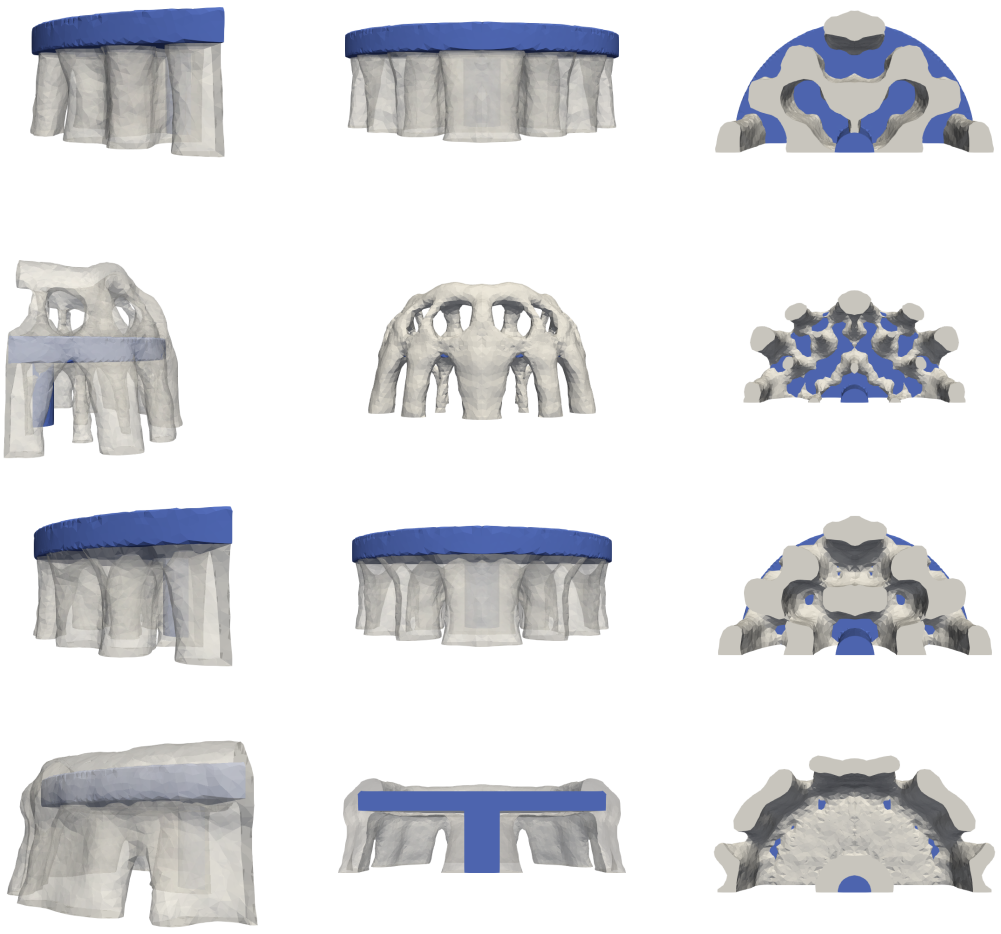

Figure 17: Different views of the optimized designs for the 3-d table: perfect interface (upper row), $\alpha = \beta = 400$ (2nd row), $\alpha = 100, \beta = 1$ (3rd row) and $\alpha = 1, \beta = 100$ (lower row).